

NE 5742 Nuclear Radiations and Their Measurements

Lab 4A & 4B Report

Chris Koellhoffer
Mark Luke

Submitted: March 22nd, 2019

I. Introduction

These labs were designed to provide more exposure to different types of gamma-ray detectors--Hyperpure Germanium (HPGe) and Cadmium Zinc Telluride (CZT) detectors, specifically--and to compare these to each other and the previously used NaI detector. Lab 4A was focused on using the HPGe detector to analyse some of the same spectra as done with the NaI in Lab 3, to show the advantages of each type. Lab 4B introduced the CZT detector as a middle ground between cheaper but less-precise NaI and the high-precision but cryogenically-cooled and cumbersome HPGe. Both labs ultimately compared the detector types, and determined which would be most suitable for a given application.

A. 4A

The following instrumentation was used: Canberra GC5019 HPGe Detector with integrated preamplifier, Canberra Lynx MCA with integrated high-voltage bias supply, and a computer with spectroscopy software. The germanium detector and first-stage amplifier in the preamp were both cooled to cryogenic temperatures using liquid nitrogen, as the sensitivity of the detector mandates such cooling to reduce Johnson noise (which is caused by thermal agitation of charge carriers in a conductor). The detector configuration is shown in Figure 1A of the appendices. Of importance for this lab is the useful energy range of Ge detectors, from about 50 KeV to upwards of 10 MeV. This, combined with the sensitivity of the detector, necessitates the built-in preamplifier.

B. 4B

The instruments used for this lab were the DSA 2000, providing a pulse height analyzer, amplifier with digital signal capture/shaping, and a high voltage bias source, and the CZT detector itself. CZT detectors are fairly small due to difficulties with crystal uniformity in growth, which limits their efficiency, but the high density and Z number of the material help offset this. CZT is light-sensitive but not affected by moisture, so enclosure is a fairly simple matter. The useful energy range of such detectors ranges from 10 KeV to about 1 MeV,

after which while detection is possible efficiency sharply drops. Energy resolution averages about 3% and so is markedly superior to NaI(Tl) systems but still inferior to HPGe detectors. Additionally the small size can be occasionally made to be an advantage by forming detector arrays, as CZT often has spatial resolutions below 1 mm and so such arrays are excellent for imaging applications.

II. Experimental Setup

A. 4A

The detector setup as shown in Figure 1A was provided with an attached shielding cylinder. Cs-137 and Co-60 sources were measured as in the previous lab, here for five-minute counting times. The resultant spectrums were used to determine photopeak energy resolutions and peak-to-Compton ratios to compare to the NaI detector results. The photopeak resolutions were later used to plot energy resolution as a function of energy, and to calibrate the MCA. Next, the Co-60 source was replaced with the Ba-133 used in Lab 3 and the energy spectrum was again recorded for five minutes. The resulting spectrum was compared to that found with the NaI detector to show the increased precision of the HPGe setup. After this, a Ra-226 source was measured--something that would have been infeasible with a NaI detector--and the energies of the three most intense photopeaks were compared to known values to determine radionuclides associated with those peaks. Finally a trinitite sample was placed in the detector and measured for five minutes, so as to identify at least two products of the Trinity test based on their gamma energies.

B. 4B

For this experiment, sources of Cd-109, Co-57, Cs-137, and Co-60 were used. Each source was placed as close to the front of the detector as possible, and counted for five minutes so as to provide a smooth spectrum with a clear peak for the primary gamma emitted by each source. After the lab, the stored spectra were examined to determine the peak energy and channel number, as well as the FWHM. The system energy response was then calibrated by plotting gamma energy versus peak channel number, and the FWHM in KeV and energy resolution for each radionuclide energy peak was then determined.

III. Results and Analysis

A. 4A:

A calibration curve was created for the HPGe detector and can be seen below.

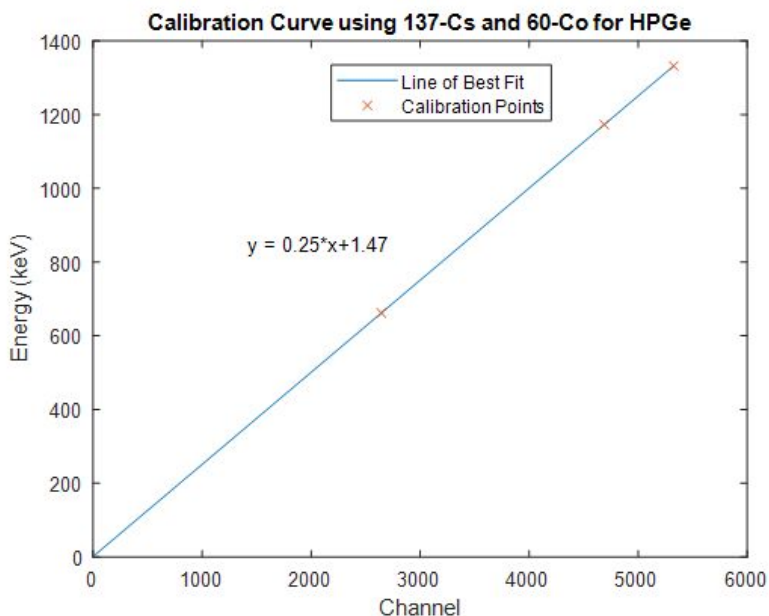


Figure 1: Calibration curve of the HPGe detector using Cs-137 and Co-60. The calibration curve had a slope of 0.2498 keV/channel and intercept of 1.47 keV. The slope was used in the next portion to determine the FWHM in terms of keV. The Full Width at Half Maximum (FWHM) and energy resolutions of each photopeak were calculated and plotted against the incident gamma ray energy. Below are the figures.

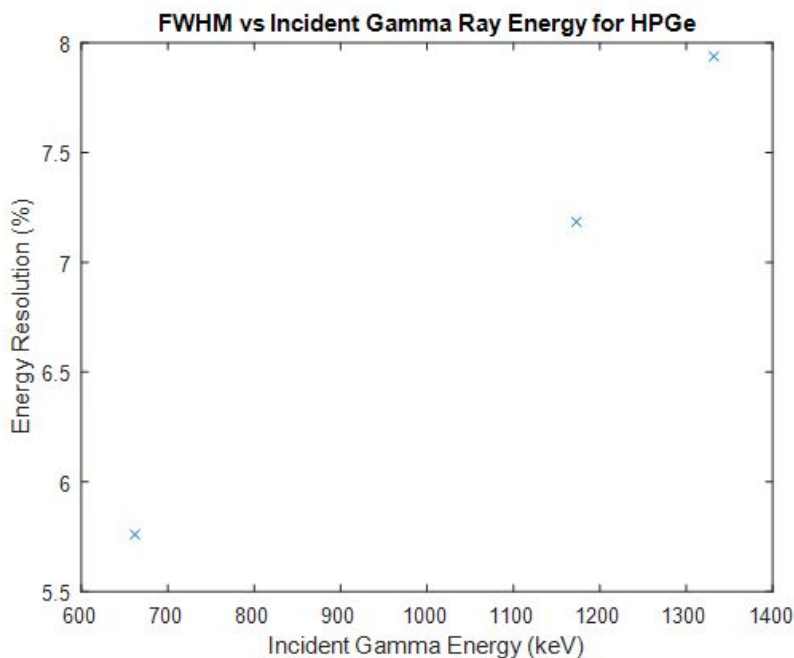


Figure 2: FWHM vs Incident Gamma Ray energy for the HPGe detector.

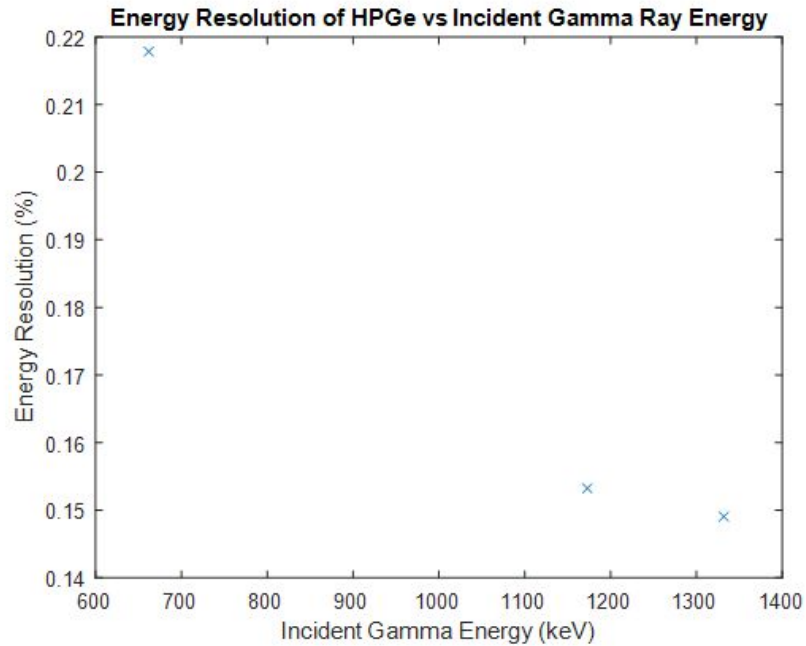


Figure 3: Energy resolution of each photopeak vs the incident gamma ray energy for the HPGe detector.

It can be seen from the graphs that the FWHM scales with the square root of the incident gamma ray energy, due to poisson uncertainty. Energy resolution scales with 1 over the square root of incident energy, as it is found by dividing the FWHM by incident energy. It makes logical sense that higher incident gamma energies produce lower energy resolutions as they are statistically more likely to create more ionizations. A summary of the FWHM, energy resolutions, and peak to compton ratios is shown below.

Table 1: FWHM, Energy Resolution and peak to compton ratios for the HPGe detector.

HPGe Detector			
	FWHM (keV)	Energy Resolution	Peak to Compton Ratio
Cs-137 662 keV	1.44	0.218	N/A
Co-60 1173 keV	1.80	0.153	N/A
Co-60 1332 keV	1.98	0.149	160

A spectrum of Ba-133 was taken with the HPGe and plotted alongside the spectrum taken by an NaI detector in a previous lab. The resulting plots are shown on the following page.

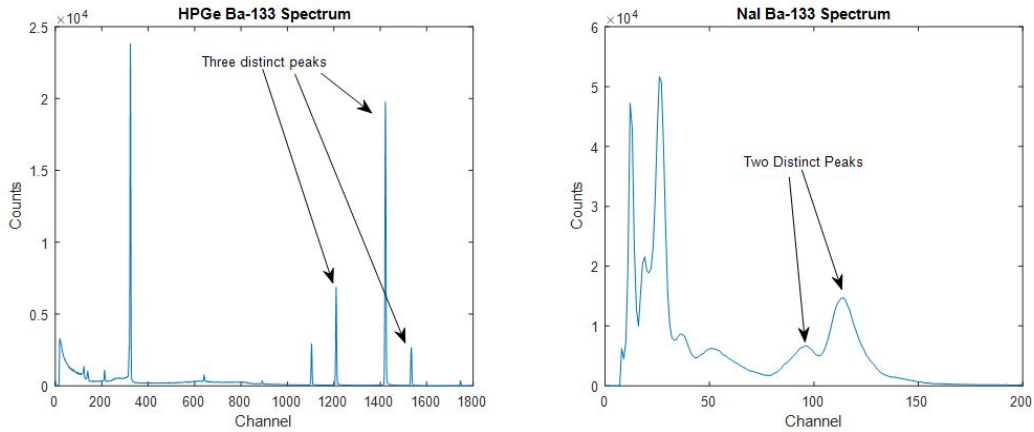


Figure 4: Ba-133 Spectrums using an HPGe and NaI detector..

The HPGe detector is clearly able to discern between the three prominent peaks produced by the Ba-133 gamma rays. The NaI detector cannot do this, as the highest energy gamma peak does not show up in the spectrum. Other peaks can be seen in the HPGe detector that are likely due to daughter products produced by Ba-133 decaying.

A spectrum of a Ra-226 source was then taken. Below is the spectrum with one daughter product identified.

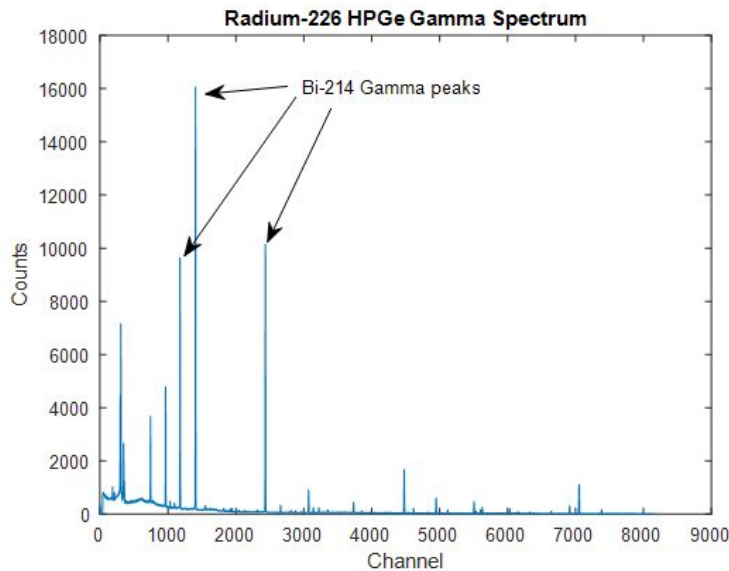


Figure 5: Ra-226 spectrum using an HPGe detector.

The three most prominent peaks belong to Bi-214 de-excitation and decay gamma rays. These correspond to energies of 609 keV, 352 keV, and 297 keV. The 609 keV gamma occurs when Bi-214 decays into Po-214, and the other two are de-excitations to Bi-214's ground state.

The gamma energies were found by multiplying the channel at which they occurred by the slope of the calibration curve.

Finally, a trinitite sample was placed on the HPGe detector and a spectrum recorded. Below is the plot with two radionuclides identified.

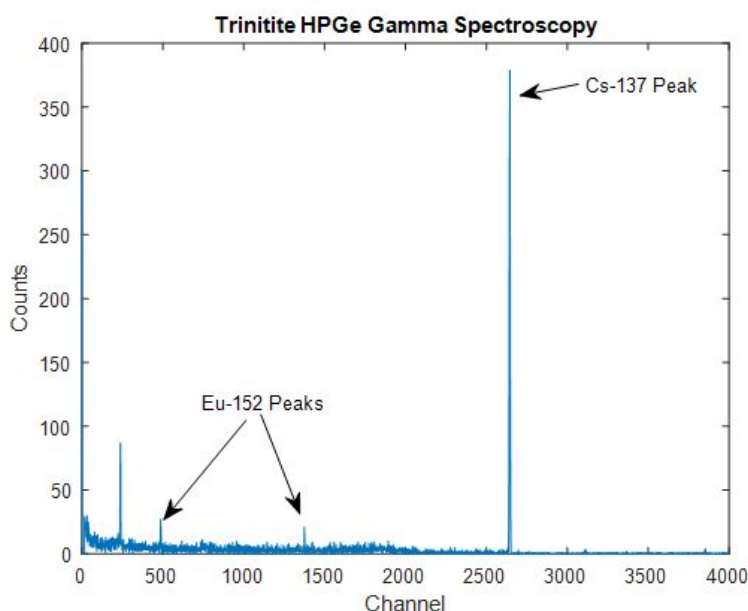


Figure 6: Trinitite gamma spectrum using a HPGe detector.

The two radionuclides identified are Europium-152 and Cesium-137. They are both products of the fission of uranium and plutonium, and have half lives long enough to last 70 years (about 12 years and 30 years, respectively). Cs-137 emits the well known 662 keV peak, and Eu-152 emits gammas at 344 and 122 keV. The third peak not identified on the plot (to the left of the initial Eu-152 peak) is likely Am-241, as it is a fission product as well and emits a 60 keV gamma which corresponds to the first peak.

The HPGe detector was shown to have great energy resolution for gammas and is able to discern between gamma rays close in energy. It would perform well for measuring activity of a sample with gamma rays at different but close energies, and for identifying a source for which there is no information. However, for measuring the activity of a monoenergetic source of gammas, an HPGe would be unnecessary and an NaI detector would work. An NaI detector would also be useful for measuring a large number of known sources to confirm the source has activity and the radionuclide it is supposed to have.

B. 4B:

A CZT detector was then utilized to measure four sources and five different gamma rays, Cd-109, Co-57, Cs-137, and Co-60. The FWHM, energy resolution, and peak channels were calculated and can be seen in the table below for each of the sources.

Table 2: CZT detector photopeak characteristics.

CZT Detector					
Radionuclide	Energy (keV)	Peak Channel Number	FWHM (Channels)	FWHM (keV)	Energy Resolution (%)
Cd-109	88	115	18.2	14.3	15.8
Co-57	122	153	18.8	14.8	12.3
Cs-137	662	840	22.7	17.8	2.69
Co-60	1173	1491	26.7	21	1.79
Co-60	1332	1694	24.5	19.3	1.45

The FWHM was found in keV by multiplying the slope of the calibration curve for the CZT detector by the FWHM in channels. The calibration curve can be seen on the following page.

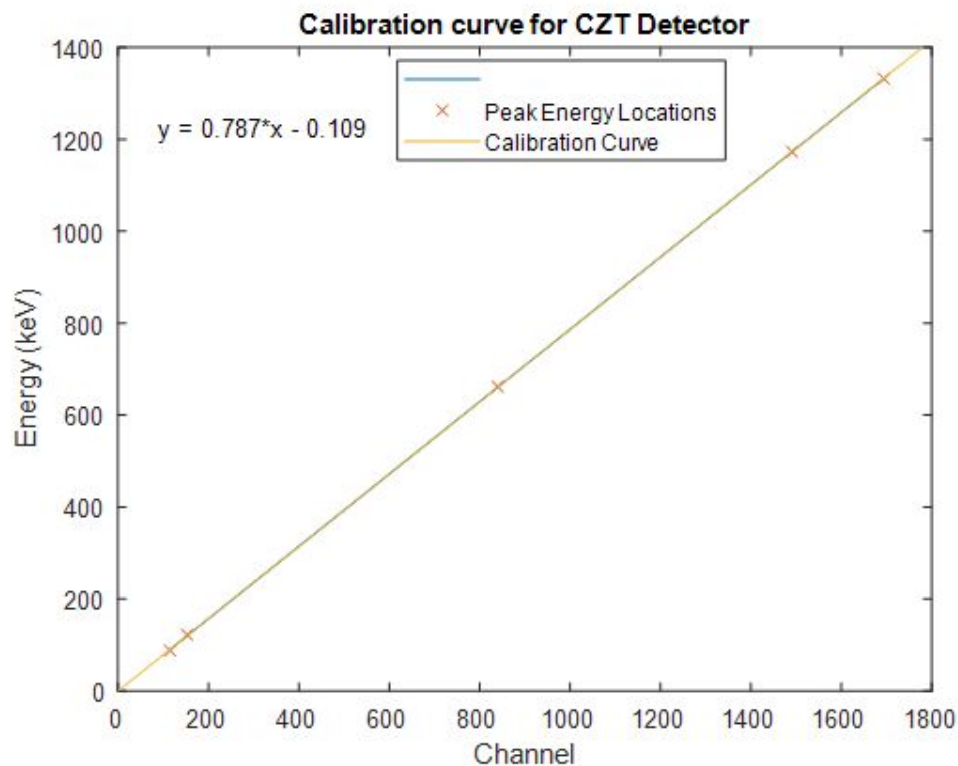


Figure 7: Calibration curve for the CZT detector.

All five sources were used in the calibration, giving a slope of 0.787 keV/channel and intercept of -0.109 keV. The R^2 value was 1 for the calibration curve. The detector response is linear with incident gamma ray energy, the same as the NaI and HPGe detectors.

FWHM and Energy resolution were plotted against incident gamma ray energy and can be seen below.

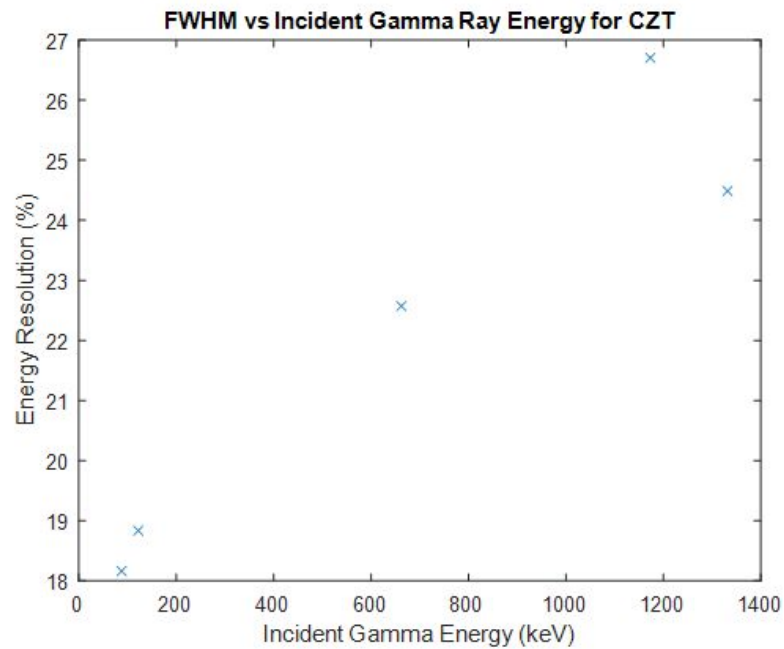


Figure 8: FWHM vs gamma ray energy for the CZT detector.

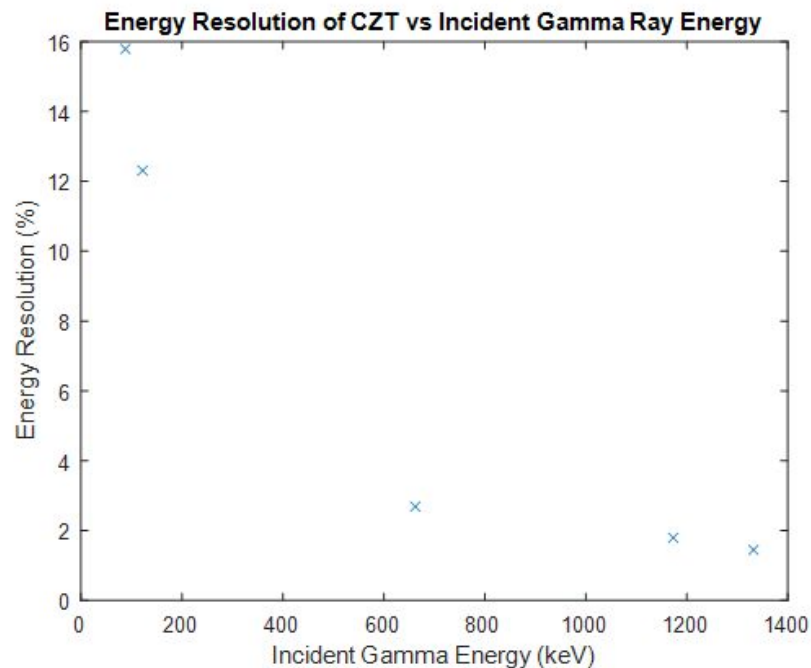


Figure 9: Energy resolution vs gamma ray energy for the CZT detector.

As seen with both the NaI and HPGe detectors before, FWHM scales with the square root of the incident gamma ray energy, due to poisson uncertainty. Energy resolution scales with 1 over the square root of incident energy, as it is found by dividing the FWHM by incident energy. A table summarizing the NaI, CZT, and HPGe detector performances for Cs-137 and Co-60 can be seen below.

Table 3: A comparison of detector characteristics.

Detector Performance Parameter	Radionuclide		
	Cs-137 662 keV	Co-60 1173 keV	Co-60 1332 keV
NaI FWHM (keV)	55.3	78.3	79.2
NaI % res	8.19	6.62	5.88
NaI peak to compton ratio	4.36	N/A	N/A
CZT FWHM (keV)	17.8	21	19.3
CZT % res	2.69	1.79	1.45
CZT peak to compton ratio	38.4	N/A	N/A
HPGe FWHM (keV)	1.44	1.8	1.98
HPGe % res	0.218	0.153	0.149
HPGe peak to compton ratio	160	N/A	N/A

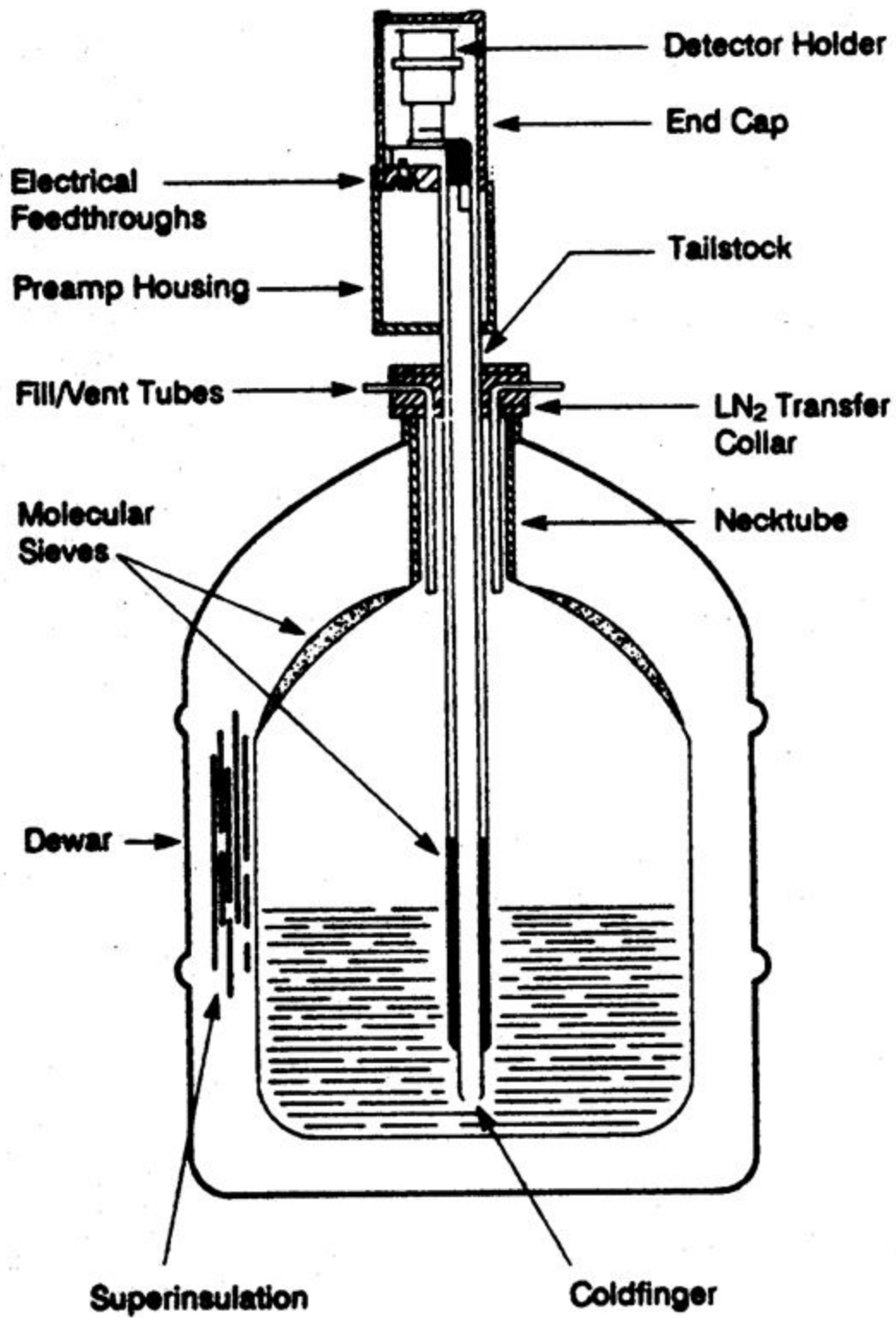
Each type of detector has its benefits and downfalls. An NaI detector could be used to survey a field for a specific radionuclide to confirm its presence, such as Cs-137. If the radionuclides in the field were not known, a CZT detector could be used to try and identify them from the different gamma energies produced as it gives better resolution than the NaI detector. An HPGe detector would not be useful in this case as it would be quite hard to carry around the liquid nitrogen required for operation. To analyze a sample that emits many different gamma energies within a lab, an HPGe would be the best choice due to its high energy resolution and ability to determine activity and quantity of source.

IV. Conclusion

The first portion of the lab demonstrated the high energy resolution of an HPGe detector. It is able to differentiate gamma rays of similar energies which allows it to identify different radionuclides within a source. Bi-214 was determined to cause the three most intense peaks from a Ra-226 source, and Eu-152 and Cs-137 were found to be in a trinitite rock from the Trinity test. Use of an HPGe detector, however, is somewhat limited to a lab environment as it must be cooled with liquid nitrogen for operation. A CZT detector was then used for these sources, as well as a source of Cd-109 and Co-57. It was seen that the CZT detector had better performance characteristics than the NaI detector, but was not great for radionuclides that emit low energy gammas. The CZT detector represents a good middle ground between NaI detectors and HPGe detectors from a mobility and gamma detection viewpoint.

Appendices

Figure 1A: HPGe Detector Setup



Plotting Code

%% NE5742 Lab 4 A and B %%

% Mark Luke %

load('NE5742_Lab4.mat')

% figure(1)

% plot(Ba133HPGe(:,1), Ba133HPGe(:,2)) %peaks between 1180 and 1250, 1400 and 1450, 1500 and 1560

% figure(2)

% plot(Cd109CZT(:,1), Cd109CZT(:,2)) %peak between 50 and 150

% figure(3)

% plot(Co57CZT(:,1), Co57CZT(:,2)) %peak between 100 and 200

% figure(4)

% plot(Co60CZT(:,1), Co60CZT(:,2)) %peaks between 1450 and 1550, 1650 and 1750

% figure(5)

% plot(Co60HPGe(:,1), Co60HPGe(:,2)) %peaks between 4600 and 4800, 5200 and 5400

% figure(6)

% plot(Cs137CZT(:,1), Cs137CZT(:,2)) %peak between 800 and 900

% figure(7)

% plot(Cs137HPGe(:,1), Cs137HPGe(:,2)) %peak between 2600 and 2700

% figure(8)

% plot(Ra226HPGe(:,1), Ra226HPGe(:,2))

% figure(9)

% plot(Trinitite(:,1), Trinitite(:,2))

% Need FWHM, energy resolution, peak to compton ratio

% of Cs-137, Co-60

[countMaxMCA137Cs, i] = max(Cs137HPGe(2600:2700,2)); %662 peak

countHalfMCA137Cs = countMaxMCA137Cs/2;

MCA137Cs_FWHM =

(Cs137HPGe(2648,1)+(countHalfMCA137Cs-Cs137HPGe(2648,2))*(Cs137HPGe(2649,1)-Cs137HPGe(2648,1))/(Cs137HPGe(2649,2)-Cs137HPGe(2648,2))) -

(Cs137HPGe(2642,1)+(countHalfMCA137Cs-Cs137HPGe(2642,2))*(Cs137HPGe(2643,1)-Cs137HPGe(2642,1))/(Cs137HPGe(2643,2)-Cs137HPGe(2642,2)));

MCA137CsresE = MCA137Cs_FWHM/Cs137HPGe(2600+i-1,1)*100;

channel137Cs = Cs137HPGe(2600+i-1,1);

[countMaxMCA60Co1, i] = max(Co60HPGe(4600:4800,2)); %1173 peak

countHalfMCA60Co1 = countMaxMCA60Co1/2;

```

MCA60Co1_FWHM =
(Co60HPGe(4693,1)+(countHalfMCA60Co1-Co60HPGe(4693,2))*(Co60HPGe(4694,1)-Co60H
PGe(4693,1))/(Co60HPGe(4694,2)-Co60HPGe(4693,2))) -
(Co60HPGe(4686,1)+(countHalfMCA60Co1-Co60HPGe(4686,2))*(Co60HPGe(4687,1)-Co60H
PGe(4686,1))/(Co60HPGe(4687,2)-Co60HPGe(4686,2)));
MCA60Co1resE = MCA60Co1_FWHM/Co60HPGe(4600+i-1,1)*100;
channel60Co1 = Co60HPGe(4600+i-1,1);

```

```

[countMaxMCA60Co2, i] = max(Co60HPGe(5200:5400,2)); %1332 peak
countHalfMCA60Co2 = countMaxMCA60Co2/2;
MCA60Co2_FWHM =
(Co60HPGe(5330,1)+(countHalfMCA60Co2-Co60HPGe(5330,2))*(Co60HPGe(5331,1)-Co60H
PGe(5330,1))/(Co60HPGe(5331,2)-Co60HPGe(5330,2))) -
(Co60HPGe(5323,1)+(countHalfMCA60Co2-Co60HPGe(5323,2))*(Co60HPGe(5324,1)-Co60H
PGe(5323,1))/(Co60HPGe(5324,2)-Co60HPGe(5323,2)));
MCA60Co2resE = MCA60Co2_FWHM/Co60HPGe(5200+i-1,1)*100;
channel60Co2 = Co60HPGe(5200+i-1,1);

```

```

% Combining both MCA data sets (137-Cs and 60-Co) to determine keV/channel
x = [channel137Cs channel60Co1 channel60Co2]; %channel number
y = [662 1173 1332]; %keV
calibcurve = polyfit(x,y,1);
figure(4)
plot(linspace(0,channel60Co2,2), polyval(calibcurve, linspace(0,channel60Co2,2)))
hold on
plot(x, y, 'x')
title('Calibration Curve using 137-Cs and 60-Co for HPGe')
xlabel('Channel')
ylabel('Energy (keV)')
legend('Line of Best Fit','Calibration Points')

```

```

Cs137_FWHMkeV = calibcurve(1)*MCA137Cs_FWHM;
Co60_1_FWHM_keV = calibcurve(1)*MCA60Co1_FWHM;
Co60_2_FWHM_keV = calibcurve(1)*MCA60Co2_FWHM;

```

```

% Peak to compton ratio for Cs-137 HPGe
low_Comp = round(358/calibcurve(1)); %finding channel of low energy compton continuum
high_Comp = round(382/calibcurve(1)); %finding channel of high energy compton continuum

```

```

avg_count = mean(Cs137HPGe(low_Comp:high_Comp, 2));

```

```

pcr = countMaxMCA137Cs/avg_count; %peak to compton ratio

```

%% Energy Resolution vs Energy

```
plot(y, [MCA137CsresE MCA60Co1resE MCA60Co2resE], 'x')
title('Energy Resolution of HPGe vs Incident Gamma Ray Energy')
xlabel('Incident Gamma Energy (keV)')
ylabel('Energy Resolution (%)')
```

```
figure(2)
plot(y, [MCA137Cs_FWHM MCA60Co1_FWHM MCA60Co2_FWHM], 'x')
title('FWHM vs Incident Gamma Ray Energy for HPGe')
xlabel('Incident Gamma Energy (keV)')
ylabel('Energy Resolution (%)')
```

%% CZT

```
[countMaxMCA137Cs, i] = max(Cs137CZT(800:900,2)); %662 peak
countHalfMCA137Cs = countMaxMCA137Cs/2;
MCA137Cs_FWHM =
(Cs137CZT(852,1)+(countHalfMCA137Cs-Cs137CZT(852,2))*(Cs137CZT(853,1)-Cs137CZT(852,1)))/(Cs137CZT(853,2)-Cs137CZT(852,2))) -
(Cs137CZT(830,1)+(countHalfMCA137Cs-Cs137CZT(830,2))*(Cs137CZT(831,1)-Cs137CZT(830,1)))/(Cs137CZT(831,2)-Cs137CZT(830,2)));
MCA137CsresE = MCA137Cs_FWHM/Cs137CZT(800+i-1,1)*100;
channel137Cs = Cs137CZT(800+i-1,1);
```

```
[countMaxMCA60Co1, i] = max(Co60CZT(1450:1550,2)); %1173 peak
countHalfMCA60Co1 = countMaxMCA60Co1/2;
MCA60Co1_FWHM =
(Co60CZT(1503,1)+(countHalfMCA60Co1-Co60CZT(1503,2))*(Co60CZT(1504,1)-Co60CZT(1503,1)))/(Co60CZT(1504,2)-Co60CZT(1503,2))) -
(Co60CZT(1476,1)+(countHalfMCA60Co1-Co60CZT(1476,2))*(Co60CZT(1477,1)-Co60CZT(1476,1)))/(Co60CZT(1477,2)-Co60CZT(1476,2)));
MCA60Co1resE = MCA60Co1_FWHM/Co60CZT(1450+i-1,1)*100;
channel60Co1 = Co60HPGe(1450+i-1,1);
```

```
[countMaxMCA60Co2, i] = max(Co60CZT(1650:1750,2)); %1332 peak
countHalfMCA60Co2 = countMaxMCA60Co2/2;
MCA60Co2_FWHM =
(Co60CZT(1704,1)+(countHalfMCA60Co2-Co60CZT(1704,2))*(Co60CZT(1705,1)-Co60CZT(1704,1)))/(Co60CZT(1705,2)-Co60CZT(1704,2))) -
(Co60CZT(1680,1)+(countHalfMCA60Co2-Co60CZT(1680,2))*(Co60CZT(1681,1)-Co60CZT(1680,1)))/(Co60CZT(1681,2)-Co60CZT(1680,2)));
MCA60Co2resE = MCA60Co2_FWHM/Co60CZT(1650+i-1,1)*100;
```

```
channel60Co2 = Co60CZT(1650+i-1,1);
```

```
[countMaxMCA57Co, i] = max(Co57CZT(100:200,2)); %122 peak
```

```
countHalfMCA57Co2 = countMaxMCA57Co/2;
```

```
MCA57Co2_FWHM =
```

```
(Co57CZT(161,1)+(countHalfMCA57Co2-Co57CZT(161,2))*(Co57CZT(162,1)-Co57CZT(161,1))/  
(Co57CZT(162,2)-Co57CZT(161,2)))) -
```

```
(Co57CZT(141,1)+(countHalfMCA57Co2-Co57CZT(141,2))*(Co57CZT(142,1)-Co57CZT(141,1))/  
(Co57CZT(142,2)-Co57CZT(141,2))));
```

```
MCA57Co2resE = MCA57Co2_FWHM/Co57CZT(100+i-1,1)*100;
```

```
channel57Co2 = Co57CZT(100+i-1,1);
```

```
[countMaxMCA109Cd, i] = max(Cd109CZT(50:150,2)); %88 peak
```

```
countHalfMCACd109 = countMaxMCA109Cd/2;
```

```
MCACd109_FWHM =
```

```
(Cd109CZT(124,1)+(countHalfMCACd109-Cd109CZT(124,2))*(Cd109CZT(125,1)-Cd109CZT(124,1))/  
(Cd109CZT(125,2)-Cd109CZT(124,2)))) -
```

```
(Cd109CZT(106,1)+(countHalfMCACd109-Cd109CZT(106,2))*(Cd109CZT(107,1)-Cd109CZT(106,1))/  
(Cd109CZT(107,2)-Cd109CZT(106,2))));
```

```
MCACd109resE = MCACd109_FWHM/Cd109CZT(50+i-1,1)*100;
```

```
channelCd109 = Cd109CZT(50+i-1,1);
```

```
x = [channelCd109 channel57Co2 channel137Cs channel60Co1 channel60Co2]; %channel  
number
```

```
y = [88 122 662 1173 1332]; %keV
```

```
calibcurve = polyfit(x,y,1);
```

```
plot(x, polyval(calibcurve, x)) %plotting line of best fit
```

```
hold on
```

```
plot(x, y, 'x')
```

```
% mdl = fitlm(x,y)
```

```
Cs137_FWHMkeV = calibcurve(1)*MCA137Cs_FWHM;
```

```
Co60_1_FWHM_keV = calibcurve(1)*MCA60Co1_FWHM;
```

```
Co60_2_FWHM_keV = calibcurve(1)*MCA60Co2_FWHM;
```

```
Co57_FWHMkeV = calibcurve(1)*MCA57Co2_FWHM;
```

```
Cd109_FWHMkeV = calibcurve(1)*MCACd109_FWHM;
```

```
% Peak to compton ratio for Cs-137 HPGe
```

```
low_Comp = round(358/calibcurve(1)); %finding channel of low energy compton continuum
```

```
high_Comp = round(382/calibcurve(1)); %finding channel of high energy compton continuum
```

```

avg_count = mean(Cs137HPGe(low_Comp:high_Comp, 2));

pcr = countMaxMCA137Cs/avg_count; %peak to compton ratio

%%

plot(y, [MCACd109resE MCA57Co2resE MCA137CsresE MCA60Co1resE MCA60Co2resE], 'x')
title('Energy Resolution of CZT vs Incident Gamma Ray Energy')
xlabel('Incident Gamma Energy (keV)')
ylabel('Energy Resolution (%)')

figure(2)
plot(y, [MCACd109_FWHM MCA57Co2_FWHM MCA137Cs_FWHM MCA60Co1_FWHM
MCA60Co2_FWHM], 'x')
title('FWHM vs Incident Gamma Ray Energy for CZT')
xlabel('Incident Gamma Energy (keV)')
ylabel('Energy Resolution (%)')

%% Barium Spectrum
%
% figure(10)
% subplot(1, 2, 1)
% plot(Ba133HPGe(:,1), Ba133HPGe(:,2))
% xlim([0 1800])
% subplot(1, 2, 2)
% plot(Ba133SpectrumNal(:,1), Ba133SpectrumNal(:,2))
% xlim([0 200])

%% Radium Spectrum

figure(8)
plot(Ra226HPGe(:,1), Ra226HPGe(:,2))

%% Trinitite Spectrum

figure(9)
plot(Trinitite(:,1), Trinitite(:,2))
xlim([0 4000])

```